Highly Porous Gold Supraparticles as Surface-enhanced Raman Spectroscopy (SERS) Substrates for Sensitive Detection of Environmental Contaminants

Seju Kang[a,b*], Wei Wang [a,b], Asifur Rahman [a,b], Wonil Nam[c], Wei Zhou[c], Peter J. Vikesland,[a,b*]

[a]Department of Civil and Environmental Engineering, Virginia Tech, Blacksburg, Virginia;

[b]Virginia Tech Institute of Critical Technology and Applied Science (ICTAS) Sustainable Nanotechnology Center (VTSuN), Blacksburg, Virginia;

[c]Department of Electrical and Computer Engineering, Virginia Tech, Blacksburg, Virginia;

[*] Corresponding authors: seju@vt.edu, pvikes@vt.edu

Postal address: 415 Durham, Virginia Tech, Blacksburg 24061, VA, USA

Keywords: *Supraparticles, surface-enhanced Raman spectroscopy (SERS), environmental contaminants, porosity, self-assembly,*

Abstract

Surface-enhanced Raman spectroscopy (SERS) has great potential as an analytical technique for environmental analyses. In this study, we fabricated highly porous gold (Au) supraparticles (i.e., ~100 μm diameter agglomerates of primary nano-sized particles) and evaluated their applicability as SERS substrates for the sensitive detection of environmental contaminants. Facile supraparticle fabrication was achieved by evaporating a droplet containing an Au and polystyrene (PS) nanoparticle mixture on a superamphiphobic nanofilament substrate. Porous Au supraparticles were obtained through removal of the PS phase by calcination at 500 °C. The porosity of the Au supraparticles was readily adjusted by varying the volumetric ratios of Au and PS nanoparticles. Six environmental contaminants (malachite green isothiocyanate, rhodamine B, benzenethiol, atrazine, adenine, and gene segment) were successfully adsorbed to the porous Au supraparticles and their distinct SERS spectra were obtained. A positive linear trend between the characteristic Raman peak intensity for each environmental contaminant and the aqueous concentration was found, thus indicating quantitative capability. The limit of detection (LOD) for the six environmental contaminants ranged from ~10 nM to ~10 μM depending on analyte affinity to the porous Au supraparticles and their intrinsic Raman cross-sections. The porous Au supraparticles enabled multiplex SERS detection and maintained comparable SERS detection sensitivity in wastewater influent. Overall, the Au supraparticles were shown to be practical SERS substrates for environmental analyses.

Graphical abstract

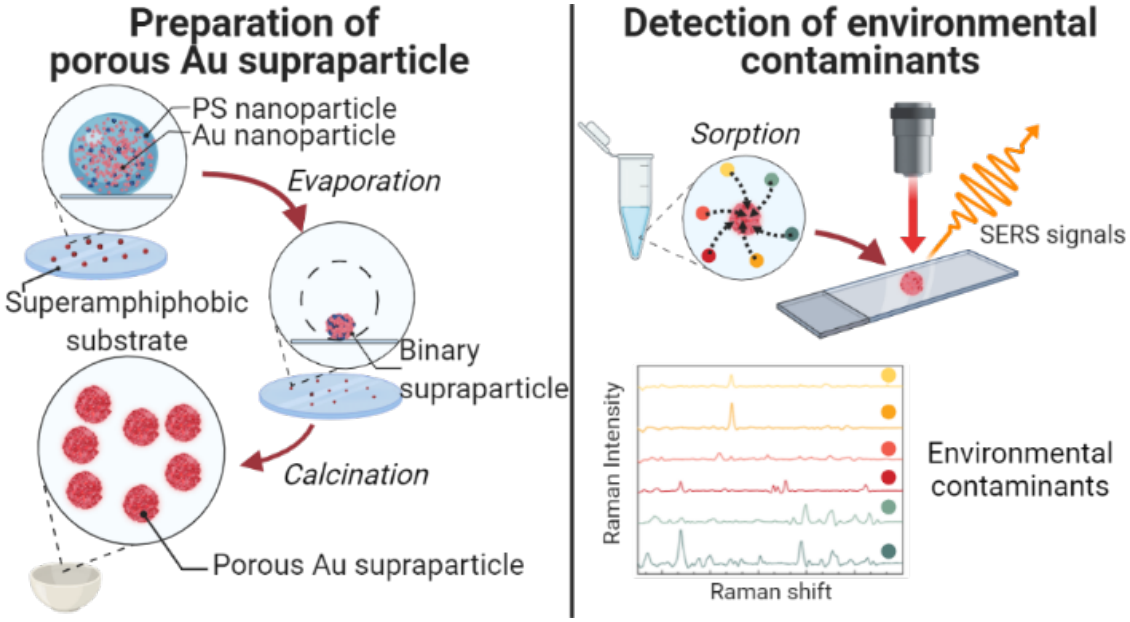

Introduction

Rapid and reliable detection of environmental contaminants is critical for the minimization of public health risks that may arise through exposure. Many analytical techniques have been developed to detect environmental contaminants such as mass spectrometry, liquid/gas chromatography, and polymerase chain reaction (PCR) based biomolecular approaches.[1–4] Although these methods are widely accepted for environmental sensing, there are still certain limitations. The major challenge of conventional analytical techniques is that most require expensive centralized facilities and professionalized expertise. Additionally, there is the need for environmental samples to be properly processed to be analyzed by such sophisticated analytical instruments (e.g., filtration, extraction, and purification) which comes with arduous labor and material costs.[5,6] These challenges can be a bottleneck for environmental analyses in resource-restrained areas (e.g., rural areas, low- and middle-income countries). In this context, the development of sensitive and rapid analytical techniques for the detection of environmental contaminants with low cost is highly desirable.

Surface-enhanced Raman spectroscopy (SERS) has shown its potential as an analytical technique with numerous applications to the environmental sector.[7–14] Inelastic Raman scattering reflects the unique fingerprint of analytes that arise from the vibrational modes of analyte chemical bonds. SERS is the phenomenon whereby the Raman signal of an analyte is significantly enhanced by a factor of 10^5-10^6 when it is situated adjacent to the surface of a plasmonic metal substrate.[15] It has been found that the localized surface plasmon resonance (LSPR) of plasmonic nanomaterials provides a near-surface enhanced electromagnetic (EM) field where the Raman signal of an analyte is significantly enhanced, this process results in “SERS hot-spots”. To achieve high sensitivity for SERS detection, it is important to create a SERS substrate with a high density of hot-spots. In prior

studies, colloidal gold (Au) nanoparticles have been used as precursors to create SERS substrates owing to their high SERS enhancement and their stability.[16] Many studies have shown that dense SERS hot-spots can be obtained by Au nanoparticle aggregation.[17–19] However, it remains a challenge to control the extent of aggregation and the association of target molecules with SERS hot-spots which influences the SERS spectrum and its intensity.[20–22]

Recently, supraparticles have attracted attention in many areas of science and technology due to their potential role in drug deployment, catalysis, energy production, and storage materials.[23] Supraparticles are agglomerates of primary micro- or nano-sized particles and have sizes of several 10 to 100 μm. Solid-state supraparticles have the benefits of facile handling and recovery in aqueous environments. More importantly, the use of supraparticles can minimize the mobility of nanoparticles that could be easily released into environmental streams. In this context, Au supraparticles as SERS substrates are expected to be advantageous for environmental analyses. Au supraparticles can not only readily provide dense SERS hot-spots from the agglomerates of Au nanoparticles, but also be easily transferred into and out of environmental samples owing to their large size and solid-state. Furthermore, a porous structure provides a large surface area, facilitating guest molecule association with the plasmonic nanoparticle surface. A porous Au supraparticle is expected to have SERS hot-spots that are highly accessible to guest molecules, thus providing excellent sensitivity.[24]

Herein, we applied a highly porous Au supraparticle for sensitive SERS detection of environmental contaminants. Fabrication of binary supraparticles was achieved by evaporating an Au and polystyrene (PS) nanoparticle mixture on a superamphiphobic liquid-repellent nanofilament substrate. Then, porous Au supraparticles were made by removing the PS phase from the binary supraparticles by calcination.[25] The porous Au supraparticles were evaluated as SERS

substrates for sensitive detection of six different environmental contaminants. In addition, the multiplex capability and applicability in an environmental matrix of the porous Au supraparticles were investigated.

Materials and Methods

Materials

All chemicals used in this study were ACS reagent or molecular biology grade. Malachite green isothiocyanate (MGITC) was purchased from Invitrogen Corp. (Grand Island, NY). Nitric acid (HNO_3), hydrochloric acid (HCl), sodium citrate tribasic dihydrate (Na_3Cit), hydrogen tetrachloroaurate hydrate ($HAuCl_4$), trichloromethylsaline (TCMS), 1H,1H,2H,2H-perfluorodecyltrichlorosilane (PFDTS), latex beads (PS nanoparticles; 600 nm mean particle size), rhodamine B (RhoB), benzenethiol (BZT), atrazine (ATZ), adenine, hexane, and toluene were purchased from Sigma-Aldrich (St. Louis, MO) and Fisher Scientific (Hampton, NH). A gene segment with 86-base length was purchased from Integrated DNA technologies Corp. (Coralville, IA) with the request of polyacrylamide gel electrophoresis (PAGE) purification. Prior to use, all glassware was washed with aqua regia – 3:1 (v:v) HCl: HNO_3. Nano-pure water (>18.2 MΩ ·cm) was used as a solvent for solution preparation unless otherwise noted.

Fabrication of Superamphiphobic Substrates

Figure 1A illustrates the fabrication of a superamphiphobic substrate following the prior literature with minor revision.[25] A silicon wafer with a diameter of 100 mm was cleaned with toluene, acetone, and ethanol to remove contaminants from the surface followed by gentle nitrogen flow drying. Then, the wafer was treated with an oxygen plasma with 30 W power for 2 mins. The wafer was incubated in a polypropylene (PP) disposable beaker containing 5 mL of toluene with 3.5 μL

of TCMS for 12 hrs while sealed with PTFE paper. Following incubation, the substrate was rinsed with hexane and dried under nitrogen. The wafer was further treated with a 120 W oxygen plasma for 2 mins and incubated in a PP disposable beaker with 5 mL of hexane with 7.5 μL of PFDTS for 30 mins sealed with PTFE paper. Then, the substrate was rinsed again with hexane and dried under nitrogen.

Preparation of Porous Gold Supraparticles

Citrate-coated Au nanoparticles were synthesized using the seed-mediated growth method.[26,27] The Au seed particles (≈13 nm) were made by boiling 100 mL of 1 mM $HAuCl_4$ and 3.88 mM Na_3Cit in a round-bottom flask on a heating mantle while refluxing for 30 mins. To synthesize larger-sized Au nanoparticles, 818 μL of Au seed particles were mixed into 100 mL of 0.254 mM $HAuCl_4$ and 0.17 mM Na_3Cit under boiling conditions. As-synthesized Au nanoparticles were filtered through a 0.22 μm PTFE filter to remove larger particles. The absorbance spectrum of the Au nanoparticle suspension was measured using an Agilent Cary 5000 UV – Vis – NIR Spectrophotometer (Santa Clara, CA). The absorbance at the peak wavelength of 533 nm was ~1.0 which is equivalent to 0.1 nM based on Beer's law. The Au nanoparticle suspension was concentrated by centrifuging 50 mL of the suspension at 2,000 ×g for 5 mins and reducing the volume to 2 mL and 2.5 nM (0.005%, volume percent). To fabricate the binary supraparticles, the Au and PS nanoparticle suspensions were mixed at volumetric ratios (*R*) of 1:5, 1:7, and 1:9 (i.e., 0.025, 0.035, and 0.045% for PS nanoparticle suspension) and further concentrated to 1% under the same centrifugation condition.

Finally, a 5 μL droplet of 1% of the Au and PS nanoparticle mixture was gently deposited onto the superamphiphobic substrate using 10-μL Eppendorf epT.I.P.S. LoRetention Reloads Tips inside a humidity-controlled chamber (**Figure 1B**). The relative humidity (RH) was maintained at

40% to control the rate of droplet evaporation. Upon complete drying, the solid-state binary supraparticles were retrieved from the substrates by slightly tilting the substrate. To remove the PS phase from the binary supraparticle and to form a porous structure, the collected supraparticles were transferred into a ceramic cubicle and calcinated in a muffle furnace at 300−500 °C for 4 hrs.

Characterization

The morphology of the Au nanoparticles was imaged using a JEOL 2100 transmission electron microscope (TEM) and the diameter was determined using ImageJ.[ref] Images of the fabricated superaphiphobic substrate surface and the morphology of the supraparticles were obtained using a JEOL IT500 scanning electron microscope (SEM). Prior to SEM imaging, the samples were coated with a 5 nm layer of iridium using a Leica ACE600 sputter coater. For the supraparticles, two elements (Au and C – representative of PS) were mapped in the SEM images using energy dispersive spectroscopy (EDS). The static contact angle of the droplet on the superaphiphobic substrate was measured using a ramé-hart Model 250 standard goniometer.

SERS detection of environmental contaminants

SERS spectra of six environmental contaminants were obtained using the porous Au supraparticles. One individual porous Au supraparticle was incubated in 100 µL of contaminant-containing solution. The sample was vortex-agitated for several hrs unless noted otherwise to allow the contaminants to adsorb to the porous Au supraparticle. After agitation, the porous Au supraparticle was transferred onto dry tissue paper. SERS spectra were obtained using a WITec Alpha500R Raman spectrometer with a 785 nm diode laser (Toptica Photonics, Germany) and a 10× objective lens. The laser power was set to 90 mW. The 300 grooves/mm grating was used, and the spectral center was set to 1500 cm^{-1}. Following microscope focusing, 400 points (20×20; X×Y) were measured across a 10 µm × 10 µm area with a 0.1 s integration time per point. The baselines of

the collected SERS spectra were subtracted using the shape function in Project Five (v. 5.0; WITec, Germany). The SERS spectra were normalized by the pseudo-peak at 77 cm^{-1} generated by a long-pass filter arising from plasmon-enhanced electronic Raman scattering (ERS). It has been reported that the Raman intensity at 77 cm^{-1} reflects the density of the SERS hot-spots such that ERS-based SERS normalization reduces spatial variations resulting from heterogenous SERS hot-spot distributions and thus enables improved SERS quantitation.[28,29]

The effects of calcination temperature and the porosity of the Au supraparticle on SERS detection of environmental contaminants were investigated using MGITC as a representative contaminant. Porous Au supraparticles prepared at different calcination temperatures (i.e., 300, 400, and 500 °C) were incubated in 1 μM MGITC solution and their SERS spectra were obtained. Additionally, porous Au supraparticles with different *R*s (i.e., 1:5, 1:7, and 1:9) were used as SERS substrates for MGITC detection. After determining the optimal calcination temperature and porosity, the porous Au supraparticles were used as SERS substrates for the detection of six environmental contaminants: MGITC, RhoB, BZT, ATZ, adenine, and an oligonucleotide gene segment. First, the kinetics of sorption of environmental contaminants to the porous Au supraparticles were monitored with extended agitation times of 1, 5, 15, 30, 45, 60, 120, and 240 mins. After the SERS spectra of environmental contaminants from the porous Au supraparticles were obtained, the times for the characteristic Raman peak intensities to plateau were determined. One characteristic peak for each SERS spectrum that exhibited the greatest Raman intensity and whose position did not overlap with others was chosen for monitoring. For biological analytes (i.e., adenine and gene segment), we introduced 1 mM $MgSO_4$ to quickly attach the molecules to the porous Au supraparticles since Mg^{2+} shields electronegativity between the Au and the analytes.[30,31] The SERS spectra for both were obtained after salt addition and 5 mins of agitation.

For sensitivity analysis, solutions with different concentrations of environmental contaminants were prepared and incubated with the porous Au supraparticles. The characteristic Raman peak intensities were plotted against the logarithmic concentrations of the environment contaminant solutions. Furthermore, multiple contaminant mixtures were incubated with the porous Au supraparticles and their SERS spectra were obtained to investigate multiplex SERS detection capability. Lastly, the SERS spectra of MGITC in wastewater influent were obtained to investigate the applicability of the porous Au supraparticles as SERS substates in an environmental matrix.

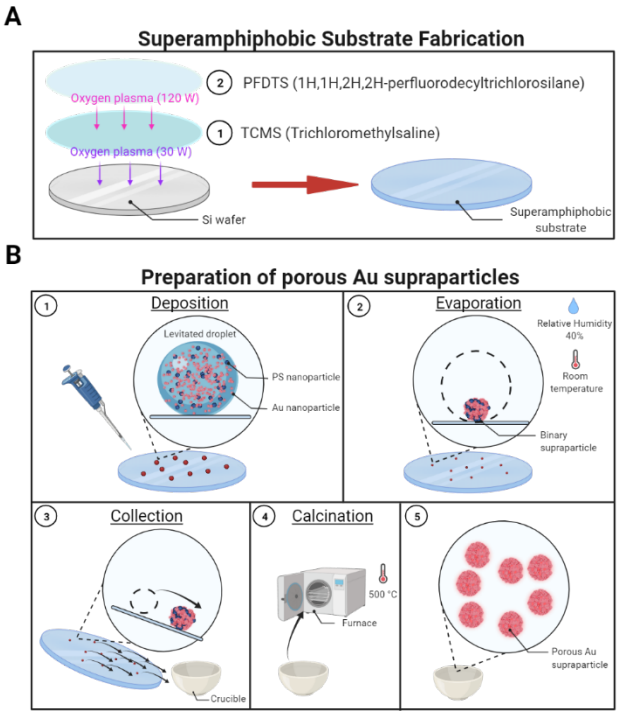

Figure 1. (A) Fabrication of the superamphiphobic substrate. (B) Preparation of the highly porous Au supraparticles. Deposition of a levitated droplet containing Au and PS nanoparticle mixture on the surface of the superamphiphobic substrates followed by evaporation in a controlled humidity chamber. After evaporation, the binary Au/PS supraparticles were collected by slightly tilting the substrate and then were calcinated in a muffle furnace at 500 °C to produce porous Au supraparticles.

Results and Discussion

Preparation of Porous Gold Supraparticles

Au nanoparticle precursors were synthesized using the seed-mediated method.[32] These Au nanoparticles exhibited a distinct LSPR peak at ~533 nm and have a spherical shape with a mean diameter of ~42.9 ± 6.2 nm (N=200) as determined by ImageJ analysis of collected TEM images (**Figure 2A** and **B**). To generate binary Au/PS supraparticles, a 5 μL droplet of an Au and PS nanoparticle suspesnion with a total volume concentration of 1% was deposited on a superamphiphobic substrate and evaporated under humidity-control. This superamphiphobic substrate was fabricated by physical and chemical surface treatment of a silicon wafer. The superamphiphobic substrate surface exhibited heterogeneously distributed nanofilaments that were coated with the fluorinated carbon from PFDTS (**Figure 2C**). The porous structure of the fluorinated carbon-coated branches provides hydrophobicity to the substrate, thus slightly levitating the mixed droplets of Au and PS above its surface (**Figure 2D**). The static contact angle of the droplet (~161.0°) confirmed the hydrophobicity of the substrate and provides a pin-free liquid contact line (**Figure 2E**). The contact angle was slightly decreased to 156.7° after 35 mins of evaporation and then dramatically decreased to 130.0° indicating the completion of evaporation (**Figure 2F**).

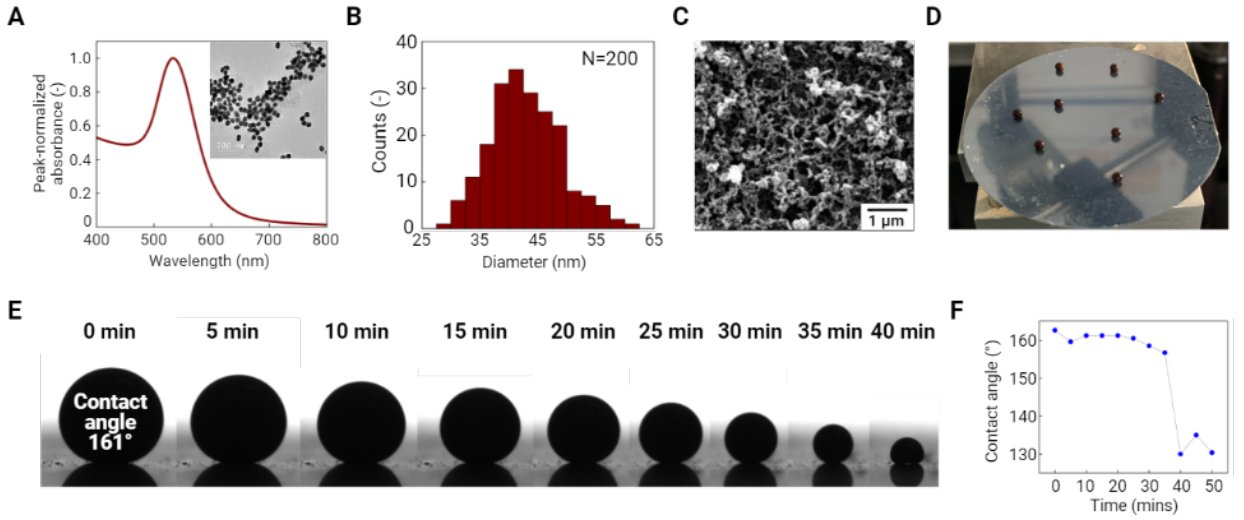

Figure 2. (A) Absorbance spectrum of the Au nanoparticle solution. Inset is the TEM image of the Au nanoparticles. (B) Histogram of TEM-determined diameter of the Au nanoparticles (N=200). (C) SEM picture of the superamphiphobic substrate surface. (D. Picture of multiple 5 µL droplets containing a mixture of Au and PS nanoparticles (volume concentration: 1%) on the superamphiphobic substrate. (E and F) Monitoring of the static contact angle change with time for a levitated droplet of Au and PS nanoparticle mixture on the superamphiphobic substrate.

After evaporation, the binary supraparticles were easily transferred onto weigh paper by slightly tilting the substrate. SEM images of supraparticles are shown in **Figure 3A**. Hollow dome-shaped supraparticles were observed with ~50 µm thick shells. During evaporation, the concentration of nanoparticles at the air-liquid interface increased, causing shell formation via colloidal assembly.[33] Unlike a nanoparticle-filled sphere, the hollow shell supraparticles are advantageous for SERS application since they have a shorter diffusion length, allowing more rapid sorption of target molecules to the Au surface.[34] SEM images of the supraparticle surface under different magnifications are shown in **Figures 3B** and **C**. These images clearly show the close-packed array of PS nanoparticles with Au nanoparticle aggregates filling the interstices between particles. Each large-sized PS nanoparticle (600 nm) was surrounded by numerous small-sized Au nanoparticles (43 nm). The colloids were distributed evenly across the surface and this can be attributed to slow evaporation since fast evaporation induced small particles to form an outer shell

with large particles enriched at the core.[35] The 50-μm thick shell consisted of multiple layers of Au nanoparticle aggregates that potentially provide a volumetric distribution of SERS hot-spots, thus enabling greater SERS enhancement.[36] In addition, the homogeneous distribution of Au and PS nanoparticles was confirmed by elemental mapping of Au and C (**Figure 3D**). This image indicates that the two elements do not overlap across the binary supraparticle surface. It was thus expected that PS phase removal would generate a large porous structure and the remaining Au-rich nanostructure can provide dense SERS hot-spots through effective LSPR coupling.[24]

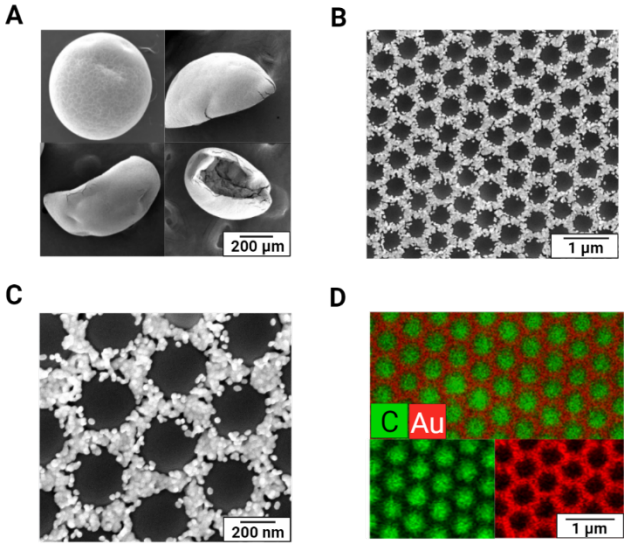

Figure 3. (A) SEM images of four-side views (top, left, bottom, right, clockwise) of binary supraparticles. (B and C) SEM images of the binary supraparticle surface under low and high magnification. (D) Elemental mapping of the supraparticle surface: overlapping (top) and C, representing PS (bottom left) and Au (bottom right) nanoparticles by energy dispersive spectroscopy (EDS). C and Au are green- and red-colored, respectively.

Effect of Calcination Temperature and Porosity

To produce a porous Au supraparticle, the PS phase in the binary supraparticle was removed by calcination. We investigated the effect of calcination temperature on the SERS performance of the porous Au supraparticles. SEM images of the porous Au supraparticle surface exhibited different

porous structures as a function of calcination temperature (**Figure 4A**). At a calcination temperature of 300 °C, PS residuals were observed in the sites of PS nanoparticles, indicating incomplete removal. At 400 and 500 °C, the SEM images indicate full removal of PS nanoparticles from the original sites. However, some of the porous structures were filled with melted PS nanoparticles at a calcination temperature of 400 °C. Such differences in the SEM images reflect the relative SERS performances of the substrates. SERS spectra of 1 μM MGITC on the Au supraparticles at different calcination temperatures were obtained (**Figure 4B**). Obvious SERS spectra of MGITC were found from the Au supraparticles produced at the higher calcination temperatures (400 and 500 °C), while minimal SERS signal was observed for the Au supraparticles produced at lower calcination temperature (300 °C). This result demonstrates that larger amounts of PS residues at low calcination temperatures impede close contact of MGITC to the Au surface, thus limiting SERS enhancement. To ensure the complete removal of PS nanoparticles in the supraparticles, we calcinated the supraparticles at 500 °C in the following experiments.

Since a porous structure provides a large surface area and facilitates analyte association with the surface, higher porosities are desirable. We optimized the porosity of the Au supraparticle by adjusting *R*. After the binary supraparticle was formed, the PS phase in the supraparticle was removed by calcination. The space formerly filled by the PS nanoparticles becomes void and acts as the porous structure of the supraparticle. Accordingly, an increased fraction of PS nanoparticles in the mixture is expected to increase the porosity of the Au supraparticle. Three *R*s (i.e., 1:5, 1:7, and 1:9) were used to make Au supraparticles with different porosities. SEM images of the porous Au supraparticle surface with different *R*s are shown in **Figure 4C**. All supraparticle surfaces exhibited clear porous structures thus indicating that the calcination of the PS nanoparticles succeeded in the formation of micropores with diameters of several 100 nm which is comparable

to the diameter of the PS nanoparticles. Three-dimensional Au porous structures were expected to exhibit a strong EM field within their volume due to effective coupling of the LSPR.[36]

To further analyze the compositional distribution of the supraparticle surface after calcination, elemental maps of the SEM images were obtained using EDS (**Figure 4D**). All supraparticle surfaces exhibited high porosity. As *R* increased, increasingly porous structures were observed. The different concentrations of PS nanoparticles in the droplet provide distinct porous structures following calcination. For an *R* of 1:5, the surface only exhibited distanced holes that reflect the spaces previously filled by PS nanoparticles. For an *R* of 1:9, most void spaces following PS nanoparticle removal were interconnected and formed a continuous porous structure, which is essential to allow guest molecules to diffuse inside the supraparticle.[25] Interestingly, in the EDS images, carbon was still observed within the porous structure along with Au. This result implies some fraction of PS remained after calcination. We suggest that the SERS signals may not be affected by PS considering its transparency and it would increase the affinity of hydrophobic analytes due to the carbon layer. The effect of the carbonized PS residues within the porous Au supraparticle on SERS detection of hydrophobic organic contaminants should be further explored.

The effect of Au supraparticle porosity on SERS performance was investigated. The SERS spectra of 1 μM MGITC on the porous Au supraparticles with different *R*s are shown in **Figure 4E**. Clear SERS spectra of MGITC were obtained from all porous Au supraparticles, thus demonstrating successful SERS detection. To investigate the SERS performance of the Au supraparticles with different porosities, characteristic Raman peak intensities were compared (**Figure 4F**). The Raman intensity at 418 cm^{-1} of MGITC on the Au supraparticles increased with an increase in *R*: 0.334 (±0.020), 0.343 (±0.013), and 0.372 (±0.025) for *Rs* of 1:5, 1:7, and 1:9.

The strong SERS performance of the porous Au supraparticles can be attributed to the existence of a large porous structure, making it much easier for MGITC to diffuse into the Au supraparticles. As a control, a pure Au supraparticle (i.e., solely 1% Au nanoparticle assembly, *R* = 1:0) was evaluated as a SERS substrate. It is worth noting that even a supraparticle made from single primary nanoparticles has naturally emergent nanoscale porosity that arises from formation of interstitial sites (i.e., the gaps between nanoparticle aggregates).[23] Nonetheless, analyte molecules will primarily associate with the outer shell due to the small size of interstitial sites. For this reason, it was hypothesized that the microscale porous structure made by PS phase removal in the binary Au/PS supraparticle would increase the accessibility of the guest molecules to inherent SERS hot-spots, resulting in better SERS performance than pure Au supraparticles. Interestingly, the Raman intensity of MGITC for the pure Au supraparticle was 0.349 ($\pm$0.011) greater than those of the Au supraparticles with the *R*s of 1:5 and 1:7. These results show that the introduction of micropores can improve the SERS performance of the porous Au supraparticles. However, the porosity should be high enough to exceed the effect of SERS enhancement by nanoscale interstitial sites from the pure Au supraparticle. Overall, the *R* of 1:9 was chosen as the optimal condition since it exhibited the best SERS performance.

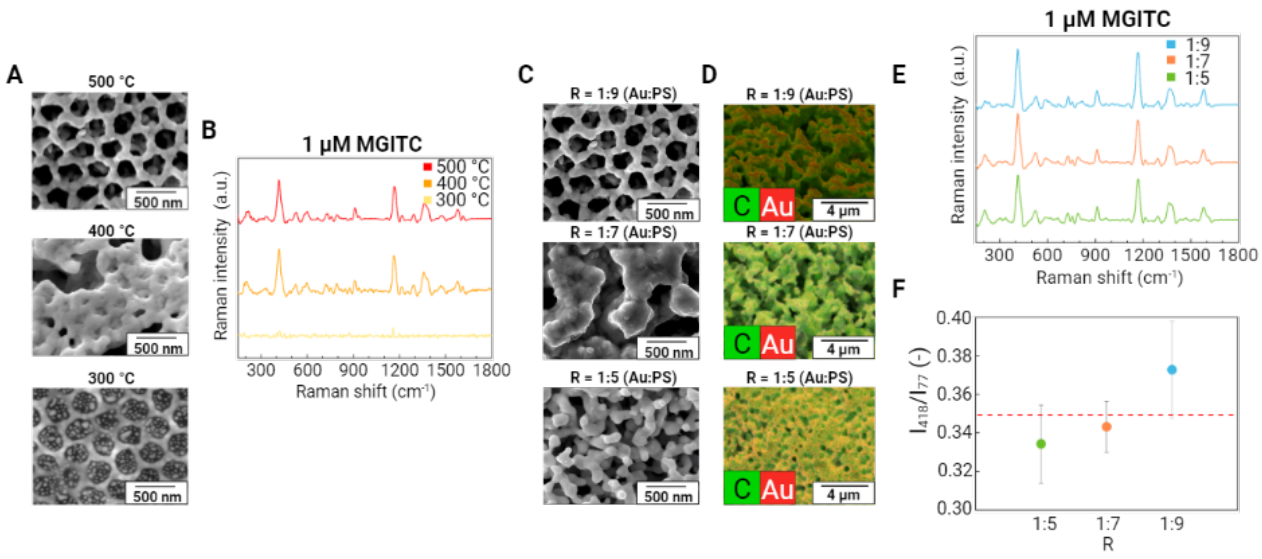

Figure 4. (A) SEM images of the porous Au supraparticles surface after calcination at different temperatures (B) Vertically stacked SERS spectra of 1 μM malachite green isothiocyanate (MGITC) were obtained from the porous Au supraparticles at different calcination temperatures. (C and D) SEM and EDS mapping images of the porous Au supraparticle surface with different volumetric ratios (*R*s) (1:5, 1:7, and 1:9 from bottom to top) between Au and PS nanoparticles in the droplet for evaporation induced self-assembly. (E) Vertically stacked SERS spectra of 1 μM MGITC from the porous Au supraparticles with different *R*s (F) Comparison of the characteristic Raman peak intensity at 418 cm^{-1} with different porosities of the Au supraparticles. The symbols and error bars indicate the means and standard deviation of the intensities from the 400 SERS spectra. Red-dashed line indicates the same peak intensity with the pure Au supraparticles.

SERS Detection of Environmental Contaminants

Based on the optimal conditions for calcination temperature and the porosity of the Au supraparticle, SERS detection of a range of environmental contaminants was explored. First, two synthetic organic dyes, MGITC and RhoB, were targeted. These chemicals are often considered omnipresent environmental contaminants due to their large-scale production and wide application in textiles, tanning, and printing.[37] Some organic dyes are non-biodegradable such that they are not easily removed by conventional wastewater treatment plants.[38] Next, two organic contaminants, BZT and ATZ, were chosen. BZT is one toxic compound widely used in the pharmaceutical industry and is classified as a priority pollutant by USEPA.[39] ATZ is an example of a herbicide

that has been widely used historically.[40] In addition, nucleic acid and its main component, adenine, were targeted. Nucleic acids are of great interest for the characterization of microbial communities and biological function in many environments. For example, integrase-integron class 1 (*int*I1) facilitates the horizon gene transfer among bacteria such that its amount has been used as a proxy to indicate the number of antibiotic resistance genes.[41] In this study, an 86-base length gene segment that is one part of *int*I1 was targeted (**Table S1**).

Owing to its porosity, the Au supraparticle can enrich environmental contaminant concentration from an aqueous solution over a certain contact period. As a result, the distinct SERS spectra of environmental contaminants were successfully obtained from the porous Au supraparticles (**Figure 5A**). The strong distinct peaks arising from various vibrational modes are listed in **Table S2**. Characteristic peaks for each SERS spectrum that exhibited the greatest Raman intensity and whose position did not overlap with others were chosen as follows: MGITC (418 cm^{-1}, out-of-plane benzene ring deformation[42]), RhoB (1194 cm^{-1}, C−C bridge band stretching[43]), BZT (1068 cm^{-1}, C−C−C bending and C−S stretching[44]), ATZ (655 cm^{-1}, the asymmetric deformation N–C–N/C–N–C and ring breathing[45]), and gene segment (730 cm^{-1}, ring breathing of adenine[46]). Since adenine is one of the main components of the gene segment along with other nucleotides (guanine, thymine, and cytosine), its SERS spectrum exhibited a similar profile to that of the gene segment.[18] Due to these two structural similarities, the same characteristic peak was chosen. **Figure 5B** shows histograms of the characteristic peak intensities for the given contaminants across the 10 μm × 10 μm scan area with 20 × 20 (X × Y) points. For all environmental contaminants, the characteristic Raman peak intensities were normally distributed across the scan area. The coefficients of variation (CV) of the characteristic peak intensities ranged from 8.9 to 37.9%, illustrating the reproducibility of the substrate.

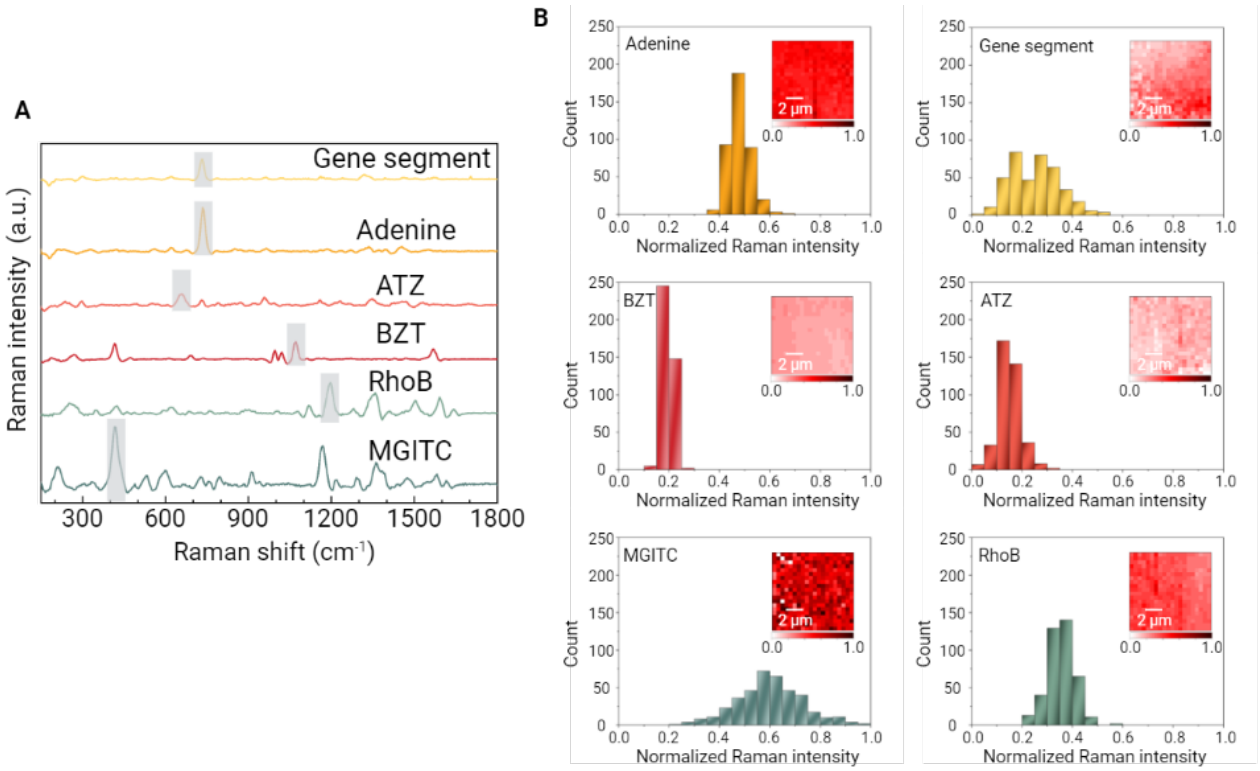

363

364 **Figure 5**. (A) Vertically stacked SERS spectra of environmental contaminants from the porous Au
365 supraparticles: malachite green isothiocyanate (MGITC; 1 μM), rhodamine B (RhoB; 100 μM),
366 benzenethiol (BZT; 10 μM), atrazine (ATZ; 1 mM), adenine (50 μM), and gene segment (50 μM).
367 The dark gray areas indicate the characteristic peaks for each spectrum (B) Histogram of the
368 normalized Raman intensity of the characteristic peak for given contaminants across a 10 μm ×
369 10 μm scan area with 20 × 20 (X × Y) points. The insets show the spatial distribution of the
370 Raman intensity across the scan area.

371

372 Due to the different affinities of the environmental contaminants to the porous Au
373 supraparticles, sorption kinetics were followed to find the time required to reach equilibrium. The
374 Raman intensities of their characteristic peaks were plotted against the contact time (**Figure S1**).
375 The sorption kinetics for adenine and gene segment were not obtained since salt-induced
376 association (i.e., electrostatics mediated association at high concentrations of $MgSO_4$) was
377 applied.[30,47] These latter samples were simply agitated for 5 mins after adding the salts to the
378 solution. For other environmental contaminants, the Raman intensities increased over time as
379 characterized by a curvilinear pattern. The results showed that the Raman intensities reached a

plateau prior to one hr for MGITC and BZT and two hrs for RhoB and ATZ, respectively. The faster sorption of MGITC and BZT was expected because they contain a thiol group that readily forms a covalent bond with the Au surface.[48]

To explore the sensitivity of the porous Au supraparticles as SERS substrates, all six environmental contaminants with different concentrations were incubated with one supraparticle for the predetermined contact periods. Following such incubation, the SERS spectra of environmental contaminants from the porous Au supraparticles were obtained. The characteristic Raman peak intensities were plotted against the logarithm of the environmental contaminants' concentrations (**Figure 6**). The clear positive linear trends between the two variables were shown with the high R-squared values (> 0.89) for all six environmental contaminants. The results demonstrate the applicability of the porous Au supraparticles for quantitative SERS analysis. Based on the best-fit linear regression equations and the standard error of the regression, the limits of detection (LODs) for the six environmental contaminants were determined.[49] Among six targets, MGITC and RhoB had the lowest LODs of 41.0 and 98.4 nM owing to their large Raman cross-sections.[50] MGITC was more sensitively detectable due to the affinity of its thiol group to the Au surface. The porous Au supraparticle in this study showed slightly better sensitivity for RhoB detection than a previously described Au nanoparticle-based approach.[51] The LODs for BZT and ATZ were 1.8 and 37.7 μM. BZT had a lower detection limit than ATZ which can also be attributed to its thiol group.

Among six targets, the most hydrophobic organic contaminant, ATZ, had the lowest sensitivity. This may reflect its low affinity to the substrate and its small Raman cross-section. We expect that increasing the hydrophobicity of the porous Au supraparticle would enable more sensitive ATZ detection. For example, pyrolysis of the PS phase (i.e., calcination without oxygen

in the air) would generate more hydrophobic Au supraparticles. Since the surface affinity of the substrate plays a central role over target selectivity in SERS[52], surface functionalization can also be applied for more sensitive ATZ detection. For example, molecularly imprinted polymer (MIP) functionalized Au nanoparticles were recently applied to achieve high selectivity against ATZ.[53] The gene segment and adenine had comparable LODs of 1.0 and 1.7 μM which is plausible based on their structural similarities. Unlike other contaminants, the SERS profiles of adenine and gene segment were quite similar. However, prior studies habe succeeded in discrimination of the SERS spectra of different gene sequences by comparing peak ratios or through use of multivariate data analysis.[18,31] Thus, discriminatory SERS detection of different gene sequences should be possible using the porous Au supraparticles.

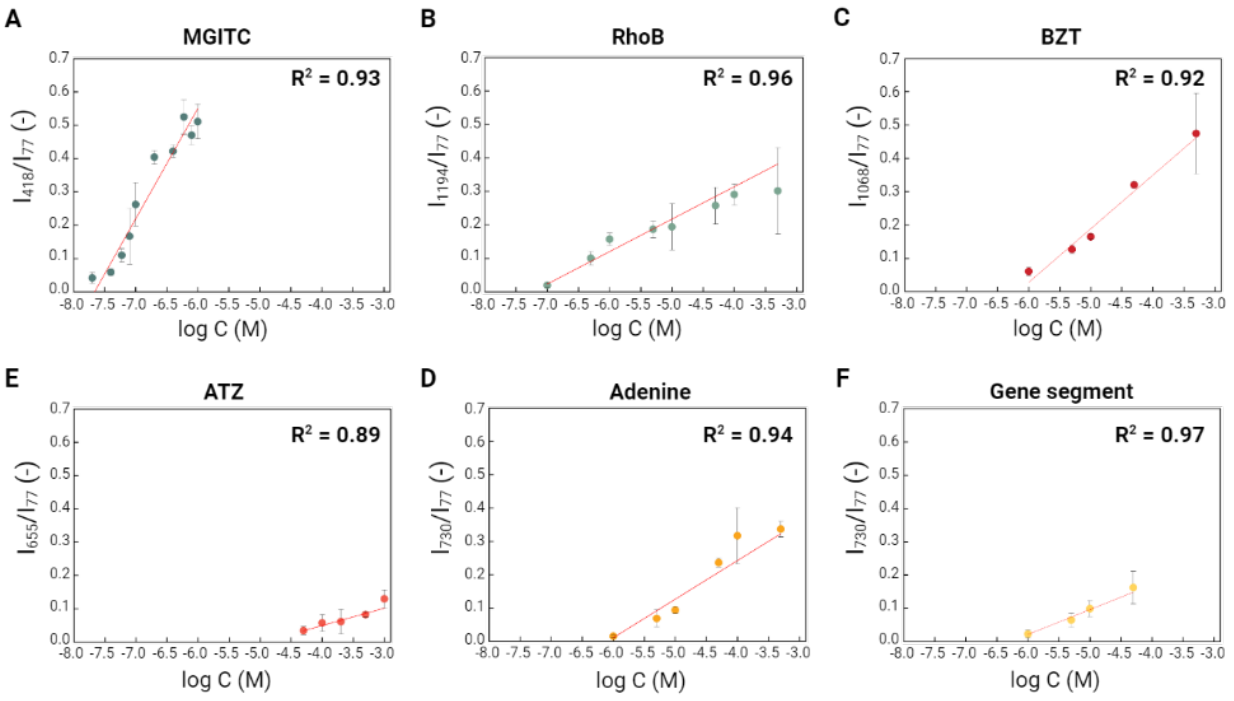

Figure 6. Sensitivity test for environmental contaminants detection using the porous Au supraparticles as SERS substrates. Plots of the characteristic Raman peak intensities against the logarithmic concentrations of the environmental contaminants. The symbols and error bars

418 indicate the means and standard deviation of the Raman peak intensities from 400 SERS spectra.
419 The best-fit linear curves were expressed as red-line with the R-squared values.
420
421 **Multiplex SERS Detection of Environmental Contaminants**

422 Because the porous Au supraparticle provides a large surface area with dense SERS hot-spots, we
423 hypothesized that it could be used to detect multiple environmental contaminants simultaneously.
424 To test such multiplexity, the SERS spectrum of a mixture containing MGITC, RhoB, and BZT
425 with concentrations of 10 nM, 10 μM, and 5 μM was obtained (**Figure 7A**, left). The relative
426 analyte concentrations were adjusted such that Raman signals from all three molecules were
427 detectable. Since every molecule has different cross-sectional Raman signals, if one molecule
428 exhibited high Raman intensity, it could block the Raman signals from others. The SERS spectrum
429 of the mixture solution exhibited some distinct peaks arising from MGITC, RhoB, and BZT. (e.g.,
430 915 cm^{-1} from MGTIC; 1197 and 1276 cm^{-1} from RhoB; 998, 1021, and 1069 cm^{-1} from BZT). In
431 addition, multiplex SERS detection of four nucleotides (adenine (A), thymine (T), guanine (G),
432 and cytosine (C)) was also investigated. The SERS spectrum of the mixture solution containing 10
433 μM of A, T, G, and C was obtained using the porous Au supraparticles (**Figure 7A**, right). The
434 SERS spectrum of the mixture solution exhibited distinct peaks arising from A, T, G, and C (e.g.,
435 730 cm^{-1} from A; 780 cm^{-1} from T; 964 and 1465 cm^{-1} from G; 800 and 1304 cm^{-1} from C). Thus,
436 confirming that the multiplex SERS detection of environmental contaminants was enabled using
437 the porous Au supraparticles.

438 **SERS Detection in Environmental Matrix**

439 To investigate applicability in real environmental matrices, the porous Au supraparticle was tested
440 in wastewater influent containing high amounts of organic matter and high ionic strengths (**Table**
441 **S3**). Different concentrations of MGITC were spiked into wastewater influent and mixed with the

Au supraparticles. The result shows the positive linear trend of the characteristic intensity of MGITC at 418 cm^{-1} in wastewater influent against the logarithmic concentration (**Figure 7B**). It seemed that each data point in wastewater influent was well-fitted within the 95% confidence band from those for MGITC in clean water. This result demonstrates there is limited interference between components in the wastewater influent on the SERS performance of the porous Au supraparticle. In addition, the porous Au supraparticle exhibited great stability in wastewater influent throughout the agitation, proving the easy recovery process after analysis.

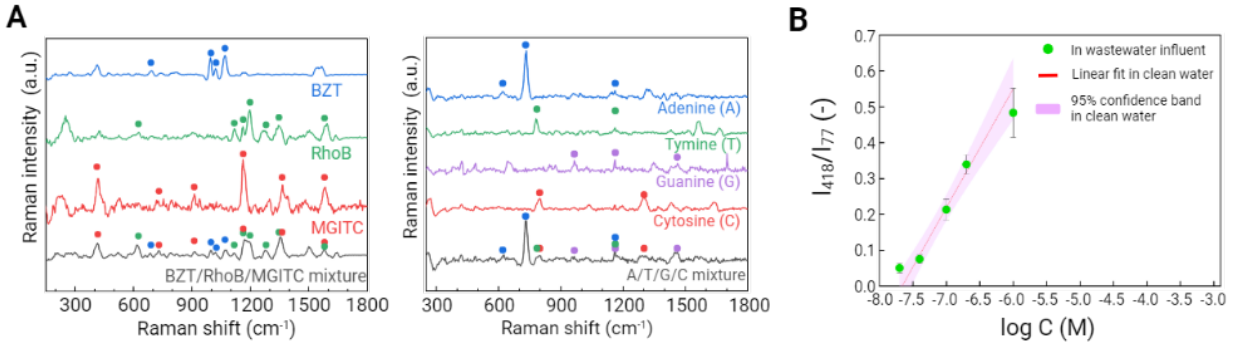

Figure 7. Multiplex SERS detection of environmental contaminants and SERS detection in environmental matrix. (A) Vertically stacked SERS spectrum of mixture solution containing 10 nM malachite green isothiocyanate (MGITC), 10μM rhodamine B (RhoB), and 5 μM of benzenethiol (BZT), and their individual spectra (left). Vertically stacked SERS spectrum of mixture solution containing 10 μM adenine (A), thymine (T), guanine (G), and cytosine (C), and their individual spectra (right). (B) Sensitivity test for MGITC detection in wastewater influent with different concentrations. The symbols and error bars indicate the means and standard deviation of the Raman peak intensity at 418 cm^{-1} from 400 SERS spectra. The best-fit linear curve and a 95% confidence band for MGITC detection in clean water were expressed as a red line and purple area.

Conclusions

In this study, the facile fabrication of highly porous Au supraparticles was achieved by droplet evaporation of an Au and PS nanoparticle mixture on a superamphiphobic substrate followed by

PS phase removal by calcination. It was found that calcination at 500 °C completely removed PS and induced high porosity in the Au supraparticle. As the volumetric ratio between Au and PS nanoparticles in the mixture increased, a higher porous structure was formed in the Au supraparticle and exhibited higher Raman intensity of adsorbed molecules. A total of six environmental contaminants were mixed with one piece of the porous Au supraparticles respectively and the distinct SERS spectrum for each target was successfully obtained with great sensitivity. In addition, the porous Au supraparticle was successfully used for multiplex detection of environmental contaminants and exhibited great applicability in the environmental matrix. Interestingly, the pure Au supraparticle also exhibited great SERS enhancement from the formation of interstitial gaps between Au nanoparticles. We suggest that micropore formation from PS phase removal in this study plays important role in the future application of the Au supraparticles since it can capture the various size of guest molecules.

The low affinity of the porous Au supraparticles to a certain target remains a challenge to detect a trace number of environmental contaminants. To expand the applicability of the porous Au supraparticles as SERS substrate for detection of environmental contaminants, additional engineering of the porous Au supraparticles would be required such as the surface functionalization or sample pre-concentration process. Overall, despite the challenge, the results in this study illustrate the great promise and strengths of the porous Au supraparticles as SERS substrates for environmental analysis. These supraparticles exhibit dense SERS hot-spots, large surface areas, and stability in the environmental matrix. In addition, it is worth noting that the porous Au supraparticle can be used as a single-particle probe with great sensitivity and convenient handling such that the sample volume can be minimized, advantageous for environmental analysis.

Acknowledgments

Funding for this work was provided through US NSF grants CBET-1705653 and CBET-2029911 to P.V. Laboratory and instrumentation support were provided by NanoEarth a node of the NSF supported NNCI (NSF award number #2025151). Additional support was provided by the Sustainable Nanotechnology Interdisciplinary Graduate Program (VTSuN IGEP) funded by the Virginia Tech Graduate School. Some icons used within the figures were sourced from Biorender.com. We thank Stephen McCartney for helping with the SEM and EDS analyses.

References

(1) Ottesen, E. A.; Hong, J. W.; Quake, S. R.; Leadbetter, J. R. Microfluidic Digital PCR Enables Multigene Analysis of Individual Environmental Bacteria. *Science (80-.).* **2006**, *314* (5804), 1464–1467. https://doi.org/10.1126/science.1131370.

(2) Richardson, S. D. Environmental Mass Spectrometry: Emerging Contaminants and Current Issues. *Anal. Chem.* **2008**, *80* (12), 4373–4402. https://doi.org/10.1021/ac800660d.

(3) Hao, C.; Zhao, X.; Yang, P. GC-MS and HPLC-MS Analysis of Bioactive Pharmaceuticals and Personal-Care Products in Environmental Matrices. *TrAC Trends Anal. Chem.* **2007**, *26* (6), 569–580. https://doi.org/10.1016/j.trac.2007.02.011.

(4) Barceló, D.; Petrovic, M. Challenges and Achievements of LC-MS in Environmental Analysis: 25 Years On. *TrAC Trends Anal. Chem.* **2007**, *26* (1), 2–11. https://doi.org/10.1016/j.trac.2006.11.006.

(5) Rubio, S.; Pérez-Bendito, D. Recent Advances in Environmental Analysis. *Anal. Chem.* **2009**, *81* (12), 4601–4622. https://doi.org/10.1021/ac900738s.

(6) Ballesteros-Gómez, A.; Rubio, S. Recent Advances in Environmental Analysis. *Anal. Chem.* **2011**, *83* (12), 4579–4613. https://doi.org/10.1021/ac200921j.

(7) Xu, S.; Tang, W.; Chase, D. B.; Sparks, D. L.; Rabolt, J. F. A Highly Sensitive, Selective, and Reproducible SERS Sensor for Detection of Trace Metalloids in the Environment. *ACS Appl. Nano Mater.* **2018**, *1* (3), 1257–1264. https://doi.org/10.1021/acsanm.7b00301.

(8) Bodelón, G.; Pastoriza-Santos, I. Recent Progress in Surface-Enhanced Raman Scattering for the Detection of Chemical Contaminants in Water. *Front. Chem.* **2020**, *8* (June), 1–8. https://doi.org/10.3389/fchem.2020.00478.

(9) Jones, S.; Pramanik, A.; Kanchanapally, R.; Viraka Nellore, B. P.; Begum, S.; Sweet, C.; Ray, P. C. Multifunctional Three-Dimensional Chitosan/Gold Nanoparticle/Graphene Oxide Architecture for Separation, Label-Free SERS Identification of Pharmaceutical

519 Contaminants, and Effective Killing of Superbugs. *ACS Sustain. Chem. Eng.* **2017**, *5* (8),
520 7175–7187. https://doi.org/10.1021/acssuschemeng.7b01351.

521 (10) Shan, J.; Zhang, Y.; Wang, J.; Ren, T.; Jin, M.; Wang, X. Microextraction Based on
522 Microplastic Followed by SERS for On-Site Detection of Hydrophobic Organic
523 Contaminants, an Indicator of Seawater Pollution. *J. Hazard. Mater.* **2020**, *400* (December
524 2019), 123202. https://doi.org/10.1016/j.jhazmat.2020.123202.

525 (11) Hong, K. Y.; de Albuquerque, C. D. L.; Poppi, R. J.; Brolo, A. G. Determination of Aqueous
526 Antibiotic Solutions Using SERS Nanogratings. *Anal. Chim. Acta* **2017**, *982*, 148–155.
527 https://doi.org/10.1016/j.aca.2017.05.025.

528 (12) Kandjani, A. E.; Sabri, Y. M.; Mohammad-Taheri, M.; Bansal, V.; Bhargava, S. K. Detect,
529 Remove and Reuse: A New Paradigm in Sensing and Removal of Hg (II) from Wastewater
530 via SERS-Active ZnO/Ag Nanoarrays. *Environ. Sci. Technol.* **2015**, *49* (3), 1578–1584.
531 https://doi.org/10.1021/es503527e.

532 (13) Huang, X.; Liu, Y.; Barr, J.; Song, J.; He, Z.; Wang, Y.; Nie, Z.; Xiong, Y.; Chen, X.
533 Controllable Self-Assembled Plasmonic Vesicle-Based Three-Dimensional SERS Platform
534 for Picomolar Detection of Hydrophobic Contaminants. *Nanoscale* **2018**, *10* (27), 13202–
535 13211. https://doi.org/10.1039/c8nr02778a.

536 (14) Halvorson, R. A.; Vikesland, P. J. Surface-Enhanced Raman Spectroscopy (SERS) for
537 Environmental Analyses. *Environ. Sci. Technol.* **2010**, *44* (20), 7749–7755.
538 https://doi.org/10.1021/es101228z.

539 (15) Stiles, P. L.; Dieringer, J. A.; Shah, N. C.; Van Duyne, R. P. Surface-Enhanced Raman
540 Spectroscopy. *Annu. Rev. Anal. Chem.* **2008**, *1* (1), 601–626.
541 https://doi.org/10.1146/annurev.anchem.1.031207.112814.

542 (16) Wei, H.; Hossein Abtahi, S. M.; Vikesland, P. J. Plasmonic Colorimetric and SERS Sensors
543 for Environmental Analysis. *Environ. Sci. Nano* **2015**, *2* (2), 120–135.
544 https://doi.org/10.1039/C4EN00211C.

545 (17) Litti, L.; Meneghetti, M. Predictions on the SERS Enhancement Factor of Gold Nanosphere
546 Aggregate Samples. *Phys. Chem. Chem. Phys.* **2019**, *21* (28), 15515–15522.
547 https://doi.org/10.1039/C9CP02015B.

548 (18) Kang, S.; Kim, I.; Vikesland, P. J. Discriminatory Detection of SsDNA by Surface-
549 Enhanced Raman Spectroscopy (SERS) and Tree-Based Support Vector Machine (Tr-
550 SVM). *Anal. Chem.* **2021**, *93* (27), 9319–9328.
551 https://doi.org/10.1021/acs.analchem.0c04576.

552 (19) Yang, S.; Dai, X.; Stogin, B. B.; Wong, T.-S. Ultrasensitive Surface-Enhanced Raman
553 Scattering Detection in Common Fluids. *Proc. Natl. Acad. Sci.* **2016**, *113* (2), 268–273.
554 https://doi.org/10.1073/pnas.1518980113.

555 (20) Wei, H.; Willner, M. R.; Marr, L. C.; Vikesland, P. J. Highly Stable SERS PH Nanoprobes
556 Produced by Co-Solvent Controlled AuNP Aggregation. *Analyst* **2016**, *141* (17), 5159–
557 5169. https://doi.org/10.1039/C6AN00650G.

558 (21) Lawson, L. S.; Chan, J. W.; Huser, T. A Highly Sensitive Nanoscale PH-Sensor Using Au
559 Nanoparticles Linked by a Multifunctional Raman-Active Reporter Molecule. *Nanoscale*

2014, *6* (14), 7971–7980. https://doi.org/10.1039/C3NR06277E.

(22) Braun, G. B.; Lee, S. J.; Laurence, T.; Fera, N.; Fabris, L.; Bazan, G. C.; Moskovits, M.; Reich, N. O. Generalized Approach to SERS-Active Nanomaterials via Controlled Nanoparticle Linking, Polymer Encapsulation, and Small-Molecule Infusion. *J. Phys. Chem. C* **2009**, *113* (31), 13622–13629. https://doi.org/10.1021/jp903399p.

(23) Wintzheimer, S.; Granath, T.; Oppmann, M.; Kister, T.; Thai, T.; Kraus, T.; Vogel, N.; Mandel, K. Supraparticles: Functionality from Uniform Structural Motifs. *ACS Nano* **2018**, *12* (6), 5093–5120. https://doi.org/10.1021/acsnano.8b00873.

(24) Liu, K.; Bai, Y.; Zhang, L.; Yang, Z.; Fan, Q.; Zheng, H.; Yin, Y.; Gao, C. Porous Au-Ag Nanospheres with High-Density and Highly Accessible Hotspots for SERS Analysis. *Nano Lett.* **2016**, *16* (6), 3675–3681. https://doi.org/10.1021/acs.nanolett.6b00868.

(25) Liu, W.; Kappl, M.; Butt, H. J. Tuning the Porosity of Supraparticles. *ACS Nano* **2019**, *13* (12), 13949–13956. https://doi.org/10.1021/acsnano.9b05673.

(26) Turkevich, J.; Stevenson, P. C.; Hillier, J. A Study of the Nucleation and Growth Processes in the Synthesis of Colloidal Gold. *Discuss. Faraday Soc.* **1951**, *11* (c), 55–75. https://doi.org/10.1039/DF9511100055.

(27) FRENS, G. Controlled Nucleation for the Regulation of the Particle Size in Monodisperse Gold Suspensions. *Nat. Phys. Sci.* **1973**, *241* (105), 20–22. https://doi.org/10.1038/physci241020a0.

(28) Nam, W.; Zhao, Y.; Song, J.; Ali Safiabadi Tali, S.; Kang, S.; Zhu, W.; Lezec, H. J.; Agrawal, A.; Vikesland, P. J.; Zhou, W. Plasmonic Electronic Raman Scattering as Internal Standard for Spatial and Temporal Calibration in Quantitative Surface-Enhanced Raman Spectroscopy. *J. Phys. Chem. Lett.* **2020**, *11* (22), 9543–9551. https://doi.org/10.1021/acs.jpclett.0c03056.

(29) Wei, H.; Leng, W.; Song, J.; Willner, M. R.; Marr, L. C.; Zhou, W.; Vikesland, P. J. Improved Quantitative SERS Enabled by Surface Plasmon Enhanced Elastic Light Scattering. *Anal. Chem.* **2018**, *90* (5), 3227–3237. https://doi.org/10.1021/acs.analchem.7b04667.

(30) Dick, S.; Bell, S. E. J. Quantitative Surface-Enhanced Raman Spectroscopy of Single Bases in Oligodeoxynucleotides. *Faraday Discuss.* **2017**, *205*, 517–536. https://doi.org/10.1039/c7fd00134g.

(31) Xu, L. J.; Lei, Z. C.; Li, J.; Zong, C.; Yang, C. J.; Ren, B. Label-Free Surface-Enhanced Raman Spectroscopy Detection of DNA with Single-Base Sensitivity. *J. Am. Chem. Soc.* **2015**, *137* (15), 5149–5154. https://doi.org/10.1021/jacs.5b01426.

(32) Brown, K. R.; Walter, D. G.; Natan, M. J. Seeding of Colloidal Au Nanoparticle Solutions. 2. Improved Control of Particle Size and Shape. *Chem. Mater.* **2000**, *12* (2), 306–313. https://doi.org/10.1021/cm980065p.

(33) Shim, W.; Moon, C. S.; Kim, H.; Kim, H. S.; Zhang, H.; Kang, S. K.; Lee, P. S.; Wooh, S. Tailoring the Morphology of Supraparticles by Primary Colloids with Different Shapes, Sizes and Dispersities. *Crystals* **2021**, *11* (2), 79. https://doi.org/10.3390/cryst11020079.

(34) Wang, Y.; Su, F.; Lee, J. Y.; Zhao, X. S. Crystalline Carbon Hollow Spheres, Crystalline

601 Carbon−SnO 2 Hollow Spheres, and Crystalline SnO 2 Hollow Spheres: Synthesis and
602 Performance in Reversible Li-Ion Storage. *Chem. Mater.* **2006**, *18* (5), 1347–1353.
603 https://doi.org/10.1021/cm052219o.

604 (35) Liu, W.; Midya, J.; Kappl, M.; Butt, H.-J.; Nikoubashman, A. Segregation in Drying Binary
605 Colloidal Droplets. *ACS Nano* **2019**, *13* (5), 4972–4979.
606 https://doi.org/10.1021/acsnano.9b00459.

607 (36) Zhang, X.; Zhang, X.; Luo, C.; Liu, Z.; Chen, Y.; Dong, S.; Jiang, C.; Yang, S.; Wang, F.;
608 Xiao, X. Volume-Enhanced Raman Scattering Detection of Viruses. *Small* **2019**, *15* (11),
609 1–8. https://doi.org/10.1002/smll.201805516.

610 (37) Tkaczyk, A.; Mitrowska, K.; Posyniak, A. Synthetic Organic Dyes as Contaminants of the
611 Aquatic Environment and Their Implications for Ecosystems: A Review. *Sci. Total Environ.*
612 **2020**, *717*, 137222. https://doi.org/10.1016/j.scitotenv.2020.137222.

613 (38) Ali, H. Biodegradation of Synthetic Dyes—A Review. *Water, Air, Soil Pollut.* **2010**, *213*
614 (1–4), 251–273. https://doi.org/10.1007/s11270-010-0382-4.

615 (39) Li, Z.; Wu, Y.; Shen, Y.; Gu, B. Simple NIR-Emitting ESIPT Fluorescent Probe for
616 Thiophenol with a Remarkable Stokes Shift and Its Application. *ACS Omega* **2020**, *5* (19),
617 10808–10814. https://doi.org/10.1021/acsomega.0c00389.

618 (40) Graymore, M.; Stagnitti, F.; Allinson, G. Impacts of Atrazine in Aquatic Ecosystems.
619 *Environ. Int.* **2001**, *26* (7–8), 483–495. https://doi.org/10.1016/S0160-4120(01)00031-9.

620 (41) Gillings, M. R.; Gaze, W. H.; Pruden, A.; Smalla, K.; Tiedje, J. M.; Zhu, Y. G. Using the
621 Class 1 Integron-Integrase Gene as a Proxy for Anthropogenic Pollution. *ISME J.* **2015**, *9*
622 (6), 1269–1279. https://doi.org/10.1038/ismej.2014.226.

623 (42) Kamińska, A.; Dzięcielewski, I.; Weyher, J. L.; Waluk, J.; Gawinkowski, S.; Sashuk, V.;
624 Fiałkowski, M.; Sawicka, M.; Suski, T.; Porowski, S.; Hołyst, R. Highly Reproducible,
625 Stable and Multiply Regenerated Surface-Enhanced Raman Scattering Substrate for
626 Biomedical Applications. *J. Mater. Chem.* **2011**, *21* (24), 8662.
627 https://doi.org/10.1039/c0jm03336g.

628 (43) Aghajani, S.; Accardo, A.; Tichem, M. Aerosol Direct Writing and Thermal Tuning of
629 Copper Nanoparticle Patterns as Surface-Enhanced Raman Scattering Sensors. *ACS Appl.*
630 *Nano Mater.* **2020**, *3* (6), 5665–5675. https://doi.org/10.1021/acsanm.0c00887.

631 (44) Madzharova, F.; Heiner, Z.; Kneipp, J. Surface-Enhanced Hyper Raman Spectra of
632 Aromatic Thiols on Gold and Silver Nanoparticles. *J. Phys. Chem. C* **2020**, *124* (11), 6233–
633 6241. https://doi.org/10.1021/acs.jpcc.0c00294.

634 (45) Bonora, S.; Benassi, E.; Maris, A.; Tugnoli, V.; Ottani, S.; Di Foggia, M. Raman and SERS
635 Study on Atrazine, Prometryn and Simetryn Triazine Herbicides. *J. Mol. Struct.* **2013**, *1040*,
636 139–148. https://doi.org/10.1016/j.molstruc.2013.02.025.

637 (46) Guerrini, L.; Krpetić, Ž.; van Lierop, D.; Alvarez-Puebla, R. A.; Graham, D. Direct Surface-
638 Enhanced Raman Scattering Analysis of DNA Duplexes. *Angew. Chemie* **2015**, *127* (4),
639 1160–1164. https://doi.org/10.1002/ange.201408558.

640 (47) Bell, S. E. J.; Sirimuthu, N. M. S. Surface-Enhanced Raman Spectroscopy (SERS) for Sub-
641 Micromolar Detection of DNA/RNA Mononucleotides. *J. Am. Chem. Soc.* **2006**, *128* (49),

15580–15581. https://doi.org/10.1021/ja066263w.

(48) Kokkin, D. L.; Zhang, R.; Steimle, T. C.; Wyse, I. A.; Pearlman, B. W.; Varberg, T. D. Au-S Bonding Revealed from the Characterization of Diatomic Gold Sulfide, AuS. *J. Phys. Chem. A* **2015**, *119* (48), 11659–11667. https://doi.org/10.1021/acs.jpca.5b08781.

(49) Shrivastava, A.; Gupta, V. Methods for the Determination of Limit of Detection and Limit of Quantitation of the Analytical Methods. *Chronicles Young Sci.* **2011**, *2* (1), 21. https://doi.org/10.4103/2229-5186.79345.

(50) Pieczonka, N. P. W.; Aroca, R. F. Single Molecule Analysis by Surfaced-Enhanced Raman Scattering. *Chem. Soc. Rev.* **2008**, *37* (5), 946. https://doi.org/10.1039/b709739p.

(51) Sun, Y.; Li, W.; Zhao, L.; Li, F.; Xie, Y.; Yao, W.; Liu, W.; Lin, Z. Simultaneous SERS Detection of Illegal Food Additives Rhodamine B and Basic Orange II Based on Au Nanorod-Incorporated Melamine Foam. *Food Chem.* **2021**, *357* (March), 129741. https://doi.org/10.1016/j.foodchem.2021.129741.

(52) Costa, J. C. S.; Ando, R. A.; Camargo, P. H. C.; Corio, P. Understanding the Effect of Adsorption Geometry over Substrate Selectivity in the Surface-Enhanced Raman Scattering Spectra of Simazine and Atrazine. *J. Phys. Chem. C* **2011**, *115* (10), 4184–4190. https://doi.org/10.1021/jp112021j.

(53) Zhao, B.; Feng, S.; Hu, Y.; Wang, S.; Lu, X. Rapid Determination of Atrazine in Apple Juice Using Molecularly Imprinted Polymers Coupled with Gold Nanoparticles-Colorimetric/SERS Dual Chemosensor. *Food Chem.* **2019**, *276*, 366–375. https://doi.org/10.1016/j.foodchem.2018.10.036.